Attenuation compensation for time-reversal imaging in VTI media

Tong Bai[1], Tieyuan Zhu[2], and Ilya Tsvankin[1]

ABSTRACT

Time reversal is a key component in reverse-time migration (RTM) and source localization using wavefield extrapolation. The successful implementation of time reversal depends on the time symmetry (reversibility) of the wave equation in acoustic and elastic media. This symmetry in time, however, is no longer valid in attenuative media, and attenuation is often anisotropic. Here, we employ a viscoelastic anisotropic wave equation that decouples the influence of energy dissipation and velocity dispersion. That equation helps compensate for anisotropic attenuation and restore the time symmetry by changing the signs of the dissipation-dominated terms in time-reversed propagation, while keeping the dispersion-related terms unchanged. We test the Q-compensated time-reversal imaging algorithm on synthetic microseismic data from a 2D transversely isotropic medium with a vertical symmetry axis (VTI). After back-propagating multicomponent data acquired in a vertical borehole, we image microseismic sources using wavefield focusing. The source excitation times are estimated by picking the maximum amplitude of the squared shear strain component ϵ_{13} at the source locations. Accounting for attenuation anisotropy produces superior source images and more accurate excitation times compared to those obtained without attenuation compensation or with purely isotropic attenuation coefficients. The algorithm is also applied to a modified BP TI model to investigate the influence of such factors as survey geometry, errors in velocity and attenuation, noise, and limited aperture.

INTRODUCTION

A fundamental property of wave propagation through elastic or acoustic media is time symmetry, which enables the application of time reversal (TR). By reversing the recorded data in time and then injecting them back into the medium, TR is supposed to focus the energy at the excitation location and time given a sufficiently wide acquisition aperture and knowledge of the medium parameters (e.g., velocities). TR is more suitable for data with a low signal-to-noise ratio than other event localization methods since it does not require picking of arrival times (Li and van der Baan, 2016). In addition to its applications in passive seismic surveys to locate and characterize seismic sources (e.g., McMechan, 1982; Gajewski and Tessmer, 2005; Larmat et al., 2006; Steiner et al., 2008; Artman et al., 2010), TR is a crucial step in reverse-time migration (RTM). Time-reversed data are injected at the receiver locations and interact with the source (forward) wavefield through the imaging condition to produce reflecting interfaces (e.g., Baysal et al., 1983; McMechan, 1983).

The time symmetry (reversibility) of acoustic and elastic (nonattenuative) wave equations is explained by the presence of only even-order time derivatives. However, seismic waves propagating in the subsurface always experience energy dissipation and velocity dispersion. Attenuation-related terms break the time symmetry in the commonly used wave equations based on either the Generalized Standard Linear Solid (GSLS) model (e.g., Bohlen, 2002; Bai and Tsvankin, 2016) or Kjartansson's constant-Q model (e.g., Carcione, 2008). These equations include first-order time derivatives or fractional time derivatives produced by the convolutional stress-strain relationship. As discussed by Zhu (2014), TR modeling of recorded viscoacoustic data through attenuative media generates a distorted source image because of additional attenuation during time reversal. Therefore, to preserve the time symmetry and reconstruct well-focused source images, it is necessary to compensate for the attenuation effect during TR modeling or back-propagation (e.g., Fink and Prada, 2001; Labyed and Huang, 2012; Ammari et al., 2013; Zhu, 2014).

Nearly constant-Q (NCQ) models (e.g., Emmerich and Korn, 1987; Carcione, 1993; Bohlen, 2002; Bai and Tsvankin, 2016) are often adopted in simulating wave propagation in viscoacoustic and viscoelastic media. A convolutional kernel, usually called the

relaxation function, relates the stress and strain fields and ensures nearly invariant Q-values within a specified frequency band, given a sufficient number of relaxation mechanisms (memory variables). Based on Kjartansson's constant-Q model, Carcione et al. (2002) and Carcione (2008) propose an alternative approach for Q-simulation that involves fractional time derivatives. Despite its advantages (accurate constant-Q function and simple parameterization), numerical implementation of that method is hampered by the need to store at least certain parts of previously computed wavefields (Carcione, 2008), which entails excessive memory requirements.

The above propagators, however, are not suitable for Q-compensation because the dissipation and dispersion operators are coupled, and amplitude compensation is inevitably accompanied by a distortion of the velocity dispersion (Zhu, 2014; Guo et al., 2016). Using Kjartansson's constant-Q model, Zhu and Harris (2014) derive a decoupled constant-Q acoustic wave equation with two separate fractional Laplacian operators accounting for amplitude dissipation and velocity dispersion. Zhu and Carcione (2014) generalize that approach for viscoelastic (but still isotropic) media. The viscoelastic propagator is implemented by Zhu (2015) and Zhu and Sun (2017) to restore the time symmetry in time-reversal imaging and RTM for isotropic attenuative models.

Laboratory experiments (Zhu et al., 2006; Best et al., 2007) confirm the existence of substantial attenuation anisotropy in the subsurface. In particular, the magnitude of the attenuation-anisotropy parameters ε_Q and δ_Q for shale rock samples can exceed unity (Zhubayev et al., 2015). Therefore, it is imperative to account for attenuation anisotropy in seismic processing (e.g., microseismic imaging) for unconventional shale reservoirs. Estimation of attenuation anisotropy can provide new physical attributes for reservoir characterization and lithology discrimination (e.g., Behura et al., 2012; Guo and McMechan, 2017).

Within the framework of the GSLS model, Bai and Tsvankin (2016) develop a time-domain finite-difference modeling algorithm for viscoelastic media with VTI symmetry for both velocity and attenuation. Employing that forward propagator, Bai et al. (2017) present a waveform-inversion methodology for VTI media, which can estimate the attenuation parameters required for anisotropic Q-compensation. Zhu (2017) extends the constant-Q modeling approach based on the fractional time derivatives (Carcione, 2008) to anisotropic viscoelastic media. However, these wave propagators include coupled effects of dissipation and dispersion, which poses a challenge for Q-compensated TR imaging. Zhu and Bai (2019) develop a formulation with fractional Laplacians for viscoelastic VTI media that decouples the attenuation terms into those responsible for amplitude loss and dispersion.

By employing the decoupled constant-Q propagator of Zhu and Bai (2019), here we develop an algorithm for Q-compensated TR imaging in viscoelastic VTI media. In particular, we demonstrate that accounting for attenuation anisotropy could significantly improve TR imaging in VTI models, which are typical for shales. First, we briefly review the properties of the decoupled (in terms of dissipation and dispersion) viscoelastic anisotropic wave equation. Next, we show how this equation can be modified to restore the time symmetry for back-propagation in the presence of both attenuation and velocity anisotropy. A synthetic test demonstrates the decoupling of dispersion and dissipation phenomena in modeling of anisotropic wavefields based on the developed formulation. Then we implement anisotropic Q-compensation during back-propagation

with the goal of spatial and temporal source localization using synthetic microseismic data. Finally, a modified BP TI model is employed to evaluate the influence of survey geometry, errors in the velocity and attenuation, etc., on microseismic source images obtained by the proposed Q-compensated TR algorithm.

METHODOLOGY

Anisotropic viscoelastic modeling based on fractional Laplacians

By employing the fractional Laplacian to approximate the fractional time derivatives, the stress (σ_{ij})-strain (ε_{ij}) relationship for attenuative VTI media can be written as (Zhu and Bai, 2019):

$$\sigma_{11} = \eta_{11} v_{11}^{2\gamma_{11}} (\epsilon_{11} + \epsilon_{33}) + (\eta_{13} v_{55}^{2\gamma_{13}} - \eta_{11} v_{55}^{2\gamma_{11}}) \epsilon_{33}$$
$$+ \tau_{11} v_{11}^{2\gamma_{11}-1} \frac{\partial(\epsilon_{11} + \epsilon_{33})}{\partial t} + (\tau_{13} v_{55}^{2\gamma_{13}-1} - \tau_{11} v_{55}^{2\gamma_{11}-1}) \frac{\partial \epsilon_{33}}{\partial t},$$
(1)

$$\sigma_{33} = \eta_{33} v_{33}^{2\gamma_{33}} (\epsilon_{11} + \epsilon_{33}) + (\eta_{13} v_{55}^{2\gamma_{13}} - \eta_{33} v_{55}^{2\gamma_{33}}) \epsilon_{11}$$
$$+ \tau_{33} v_{33}^{2\gamma_{33}-1} \frac{\partial(\epsilon_{11} + \epsilon_{33})}{\partial t} + (\tau_{13} v_{55}^{2\gamma_{13}-1} - \tau_{33} v_{55}^{2\gamma_{33}-1}) \frac{\partial \epsilon_{11}}{\partial t},$$
(2)

and

$$\sigma_{13} = \eta_{55} v_{55}^{2\gamma_{55}} 2\epsilon_{13} + \tau_{55} v_{55}^{2\gamma_{55}-1} \frac{\partial(2\epsilon_{13})}{\partial t}, \quad (3)$$

where

$$\eta_{ij} = C_{ij}^0 \cos^2\left(\frac{\pi\gamma_{ij}}{2}\right)(\omega_0)^{-2\gamma_{ij}} \cos(\pi\gamma_{ij})(-\nabla^2)^{\gamma_{ij}}, \quad (4)$$

$$\tau_{ij} = C_{ij}^0 \cos^2\left(\frac{\pi\gamma_{ij}}{2}\right)(\omega_0)^{-2\gamma_{ij}} \sin(\pi\gamma_{ij})(-\nabla^2)^{\gamma_{ij}-\frac{1}{2}}, \quad (5)$$

and

$$\gamma_{ij} = \frac{1}{\pi}\tan^{-1}\left(\frac{1}{Q_{ij}}\right). \quad (6)$$

Here ω_0 is the reference frequency, which should be larger than the dominant frequency of the source signal, C_{ij}^0 are the stiffness coefficients defined at the frequency ω_0, Q_{ij} are the elements of the VTI quality-factor matrix (Zhu and Tsvankin, 2006), $v_{11} = \sqrt{C_{11}^0/\rho}$, $v_{33} = \sqrt{C_{33}^0/\rho}$, and $v_{55} = \sqrt{C_{55}^0/\rho}$ (v_{11}, v_{33}, v_{55} are the velocities of the horizontally traveling P-wave and vertically traveling P- and S-waves, respectively), and ∇^2 denotes the Laplacian operator. To describe the attenuation of P- and SV-waves in VTI media, it is convenient to use the Thomsen-style attenuation parameters A_{P0}, A_{S0}, ε_Q, and δ_Q instead of the elements Q_{ij} (Appendix A).

The terms multiplied with η_{ij} and τ_{ij} in equations 1–3 account for the dispersion and dissipation, respectively. Note that with $\gamma_{ij} = 0$ in equations 4 and 5, we obtain $\eta_{ij} = C_{ij}^0$ and $\tau_{ij} = 0$ ($ij = 11, 13, 33, 55$), and equations 1–3 describe a purely elastic

(nonattenuative) VTI medium. On the other hand, setting $\gamma_{ij} = 0$ only in equation 4 eliminates the velocity dispersion, while setting $\gamma_{ij} = 0$ only in equation 5 removes the dissipation. A more detailed description of the decoupled viscoelastic VTI wave equation can be found in Zhu and Bai (2019).

Viscoelastic time-reversal imaging

To implement time reversal, we replace the time t in equations 1–3 with $T - \hat{t}$, where T is the total recorded time and $\hat{t}$ is the time variable for reverse propagation. The new system described by $\hat{t}$ does not coincide with the original equations 1–3 because of the presence of the first-order time derivative in the terms controlling the amplitude dissipation. To preserve the time symmetry, we need to boost the amplitude during back-propagation, whereas the dispersion relationship should remain the same (Zhu, 2014). Hence, we change the sign in front of the dissipation-related operators (the terms containing τ_{ij}) in equations 1–3:

$$\begin{aligned}
\sigma_{11} = {}& \eta_{11} v_{11}^{2\gamma_{11}} (\epsilon_{11} + \epsilon_{33}) + (\eta_{13} v_{55}^{2\gamma_{13}} - \eta_{11} v_{55}^{2\gamma_{11}}) \epsilon_{33} \\
& - \tau_{11} v_{11}^{2\gamma_{11}-1} \frac{\partial(\epsilon_{11} + \epsilon_{33})}{\partial t} - (\tau_{13} v_{55}^{2\gamma_{13}-1} - \tau_{11} v_{55}^{2\gamma_{11}-1}) \frac{\partial \epsilon_{33}}{\partial t},
\end{aligned}$$

(7)

$$\begin{aligned}
\sigma_{33} = {}& \eta_{33} v_{33}^{2\gamma_{33}} (\epsilon_{11} + \epsilon_{33}) + (\eta_{13} v_{55}^{2\gamma_{13}} - \eta_{33} v_{55}^{2\gamma_{33}}) \epsilon_{11} \\
& - \tau_{33} v_{33}^{2\gamma_{33}-1} \frac{\partial(\epsilon_{11} + \epsilon_{33})}{\partial t} - (\tau_{13} v_{55}^{2\gamma_{13}-1} - \tau_{33} v_{55}^{2\gamma_{33}-1}) \frac{\partial \epsilon_{11}}{\partial t},
\end{aligned}$$

(8)

and

$$\sigma_{13} = \eta_{55} v_{55}^{2\gamma_{55}} 2\epsilon_{13} - \tau_{55} v_{55}^{2\gamma_{55}-1} \frac{\partial(2\epsilon_{13})}{\partial t}.$$

(9)

If the time t in equations 7–9 is replaced with $T - \hat{t}$, the expressions for σ_{11}, σ_{33}, and σ_{13} become identical to equations 1–3. This means that the time symmetry of the viscoelastic system can be restored by employing the modified equations 7–9 and amplifying the amplitudes during back-propagation.

To avoid instability that may be caused by enhancing high-frequency noise in the data, we apply a low-pass Tukey taper to the dissipation-related terms during time-reversal modeling. The taper parameters (cutoff frequency and taper ratios) are data-dependent.

The proposed methodology of Q-compensated time-reversal imaging represents an extension to viscoelastic VTI media of the approach by Zhu (2014, 2015). Here, we focus on the influence of attenuation anisotropy on Q-compensated time-reversal imaging of microseismic sources.

NUMERICAL EXAMPLES

Decoupling of dissipation and dispersion

To study the decoupled dissipation and dispersion effects, we excite the wavefield by an explosive source embedded in a homogeneous VTI medium. Because the focus here is on the influence of attenuation (rather than velocity) anisotropy, we set the Thomsen velocity parameters ε and δ at the reference frequency to zero, while the magnitude of the attenuation-anisotropy parameters is relatively large: $\varepsilon_Q = -0.6$ and $\delta_Q = -1.5$ (such negative values have been observed in labora-

tory experiments). The top two panels in Figure 1 show the displacement generated in the reference elastic medium (a) and in the fully attenuative (i.e., that with both dispersion and dissipation) model (b). The bottom panels display the wavefield obtained by including only dissipation (c) or dispersion (d). As expected, the dissipation operator significantly reduces the amplitudes in Figures 1b and 1c. In contrast, the dispersion operator only delays the wavefronts in Figures 1b and 1d, especially near the vertical direction.

The variation of amplitude with angle shown in Figures 1b and 1c is in good agreement with the linearized P-wave quality factor $Q_P = 1/(2A_P)$ (see Appendix A) derived by Zhu and Tsvankin (2006):

$$Q_P(\theta) = Q_{P0}(1 - \delta_Q \sin^2 \theta \cos^2 \theta - \varepsilon_Q \sin^4 \theta). \quad (10)$$

For negative ε_Q and δ_Q used in Figure 1, the factor Q_P increases away from the vertical up to angles close to 65° and then decreases toward 90° (Figure 2).
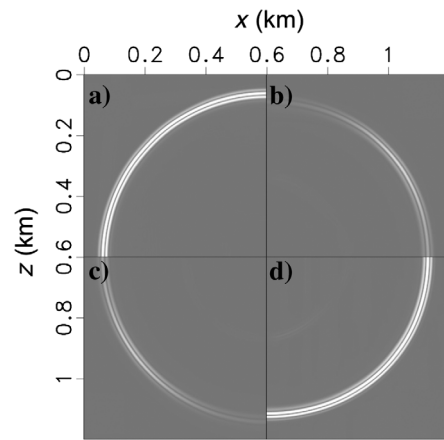

Figure 1. Amplitude snapshots of the wavefield from an explosive source located at the center of a homogeneous VTI model. The wavefield is computed for: (a) reference elastic medium; (b) fully viscoelastic medium; (c) dissipation-only medium; (d) dispersion-only medium. The parameters are: $V_{P0} = 2$ km/s, $V_{S0} = 1$ km/s, $\varepsilon = 0$, $\delta = 0$, $Q_{P0} = 20$, $Q_{S0} = 50$, $\varepsilon_Q = -0.6$, $\delta_Q = -1.5$, and $\rho = 2.0$ g/cm^3. The source excites a Ricker wavelet with a central frequency of 100 Hz (the reference angular frequency $\omega_0 = 2000$ rad/s).
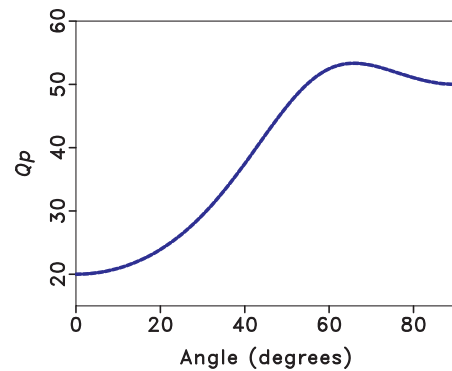

Figure 2. Linearized P-wave quality factor as a function of the phase angle (equation 10) for the model from Figure 1 ($Q_{P0} = 20$, $\varepsilon_Q = -0.6$, and $\delta_Q = -1.5$).

The dispersion-related wavefront delay in Figures 1b and 1d is also anisotropic: the P-wavefront is visibly faster in the horizontal and oblique directions than in the vertical direction (Figure 3). Similar observations are made by Galvin and Gurevich (2015), who study dispersion due to wave-induced fluid flow in fractured media. In the intermediate frequency range where the dispersion is significant, the P-wave velocity differs in the directions parallel and perpendicular to aligned fractures, whereas at high frequencies the two velocities coincide (see Figure 2 in Galvin and Gurevich, 2015). Likewise, in our model we assume no velocity anisotropy at the high reference frequency, for which $\varepsilon = \delta = 0$. Note that although we use an explosive source and assume no velocity anisotropy at high frequencies, attenuation anisotropy causes angle-dependent velocity dispersion, which produces a relatively weak SV-wave arrival (Figure 3).

Next, we conduct time-reversal imaging of synthetic microseismic data to demonstrate the need to apply anisotropic Q-compensation in attenuative VTI media. The absorbing boundary condition is applied at all model boundaries. Time reversal is applied in four different ways (Table 1): (1) elastic TR of elastic data (ETR); (2) elastic TR (i.e., no Q-compensation) of viscoelastic data (NVTR), (3) viscoelastic TR with isotropic Q-compensation using the actual quality factors Q_{P0} and Q_{S0}, while $\varepsilon_Q = \delta_Q = 0$ (IVTR), and (4) viscoelastic TR that compensates for the actual anisotropic

attenuation (AVTR). The letter "V" stands for the viscoelastic VTI model used to generate the data.

Time-reversal imaging for a layered VTI model

First, we consider a layered VTI medium in Figure 4. All three layers have significant attenuation anisotropy, and layers 2 and 3 have moderate values of the velocity-anisotropy coefficients ε and δ typical for shales (Table 2). The higher P-wave attenuation compared to that for S-waves in the second and third layers may correspond to gas-saturated shales (Qi et al., 2017). The wavefields are excited by three dislocation sources with different magnitudes of the moment tensor. Figure 5 displays the horizontal displacement generated in the reference elastic medium (Figure 5a) and the actual viscoelastic VTI model (Figure 5b). Both energy dissipation and dispersion-caused time delay are clearly visible in Figure 5b, especially for later arrivals.

Next, we reverse the data in time and inject them back into the medium to localize the sources. Because we use dislocation-type sources described by the moment tensor with only one nonzero component (M_{13}), the maximum amplitude of the squared shear
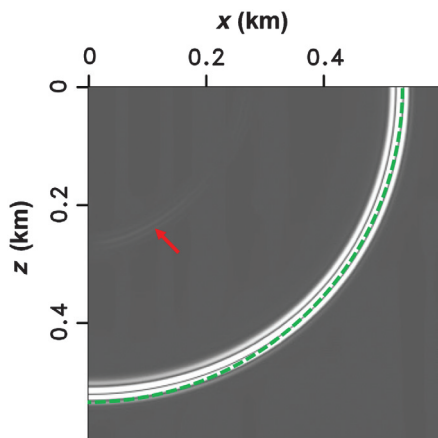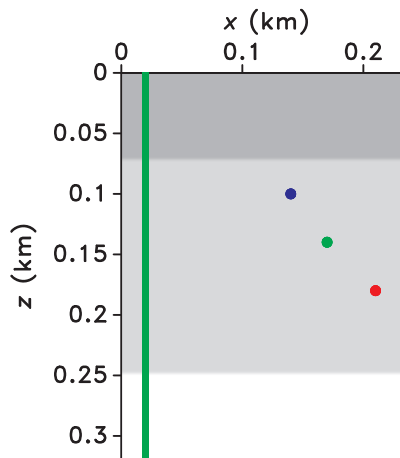

Figure 3. Zoom of Figure 1d, which shows the wavefield in a dispersion-only VTI medium. The green dashed line marks the isotropic P-wavefront; the red arrow points to the SV-wave excited due to the angle-dependent velocity dispersion.

Figure 4. Geometry of a synthetic microseismic survey in a three-layer VTI medium. The model size is 240 m × 320 m, with the grid spacing $\Delta x = \Delta z = 0.4$ m; the interval parameters are listed in Table 2. Three dislocation sources (marked by dots) with non-zero moment-tensor components $M_{13} = 600$ GPa, 800 GPa, and 1200 GPa (from left to right) are initiated at the origin times equal to 24 ms, 12 ms, and 3 ms, respectively; the central frequency of the source signal is 250 Hz. The green line at $x = 20$ m marks the receiver array.

Table 1. Types of data and models used for time reversal in the numerical examples.

	Abbreviation	Data	Model for TR
(1)	ETR	elastic	elastic
(2)	NVTR	viscoelastic	elastic
(3)	IVTR	viscoelastic	viscoelastic (isotropic Q)
(4)	AVTR	viscoelastic	viscoelastic (anisotropic Q)

Note: The viscoelastic data are computed for the models in Figures 4 and 9, which include both velocity and attenuation anisotropy.

Table 2. Interval parameters of the VTI model from Figure 4.

Layer	V_{P0} (km/s)	V_{S0} (km/s)	ε	δ	ρ (g/cm³)	Q_{P0}	Q_{S0}	ε_Q	δ_Q
1	2.0	1.2	0.1	0.05	2.0	40	30	−0.3	−0.2
2	2.5	1.25	0.2	0.15	2.2	20	50	−0.6	−1.2
3	2.8	1.5	0.25	0.18	2.4	30	60	−0.4	−0.8

Note: The velocity parameters V_{P0}, V_{S0}, ε, and δ correspond to the real parts of the stiffnesses C_{ij} defined at an angular reference frequency of 10000 rad/s.

strain ϵ_{13}^2 is chosen as the imaging condition (Kremers et al., 2011). Figure 6a shows the reference image with accurate source locations obtained by elastic TR of the elastic data (ETR, see Figure 5a). Then, we apply the same elastic TR algorithm to the viscoelastic data in Figure 5b (NVTR). As expected, the source images are blurry and mispositioned because of the uncompensated attenuation effect (Figure 6b). Next, we correct for attenuation during back-propagation, but under the isotropic *Q*-assumption (IVTR). We expect an overcompensation for P-waves and undercompensation for SV-waves based on the angle dependence of the quality factors of both modes in the second layer (Figure 7). The source images are somewhat smeared, have a lower magnitude, and are shifted (especially the right two) from their actual positions (Figure 6c). Finally, taking the attenuation anisotropy into account (AVTR) allows us to obtain well-focused and accurately positioned images of all three sources (Figure 6d), with the quality comparable to that of the reference ETR result (Figure 6a).

Using the obtained source locations, we can also estimate the corresponding excitation (origin) times. Here, following Kremers et al. (2011), the excitation time is found by picking the maximum value of the integral $E_S = \int_s \epsilon_{13}^2 dS$, where S is the area surrounding the source location with a radius of 4 m (the approximate P- and SV-wavelengths are 10 m and 5 m, respectively). The time evolution of the field E_S using different TR algorithms is displayed in Figure 8. In the reference ETR experiment, all three calculated peaks of the evolution curves are close to the actual excitation times (Figure 8a). Ignoring the influence of attenuation in TR (NVTR) leads to significant distortions (Figure 8b), and the magnitude of E_S is much lower. By choosing a relatively small window to evaluate E_S,

we assume a priori knowledge of the approximate source location. The small window size mitigates the influence of the amplified unfocused energy outside the source area produced by inaccurate *Q*-compensation. This explains the satisfactory result obtained by IVTR (Figure 8c), with the exception of the "red" source (Figure 4), which is most influenced by inaccurate *Q*-compensation. Finally, AVTR produces time-evolution curves (Figure 8d) that are similar to the reference ones (Figure 8a) and accurate estimates of the excitation times. Increased uncertainty in the source location (i.e., a larger window used to compute E_S) leads to significant deterioration in the excitation times estimated by IVTR, while the AVTR results remain accurate (not shown).

Time-reversal imaging for a modified BP section

In this section, we test the *Q*-compensated TR imaging algorithm on microseismic data simulated for a modified section of the BP TI model. The attenuation parameters are generated by scaling the velocity parameters as follows: $Q_{P0} = 1.25Q_{S0} = 8V_{P0}$ (V_{P0} in km/s), $\varepsilon_Q = -2\sqrt{\varepsilon}$, and $\delta_Q = -10\delta$ (Figure 9). The black dots in Figure 9a are dislocation sources (with the only nonzero moment-tensor component M_{13} that ranges between 2800 and 5000 GPa), which excite a Ricker wavelet with the central frequency from 100 to 110 Hz. As in the previous example, we back-propagate the modeled data to focus the wavefield at the source locations. We conduct six different tests (Table 3) to assess the influence of such factors as the survey geometry (direction and aperture), noise, and errors in velocity and attenuation, on the performance of the TR imaging algorithm. As before, each test includes the four TR applications listed in
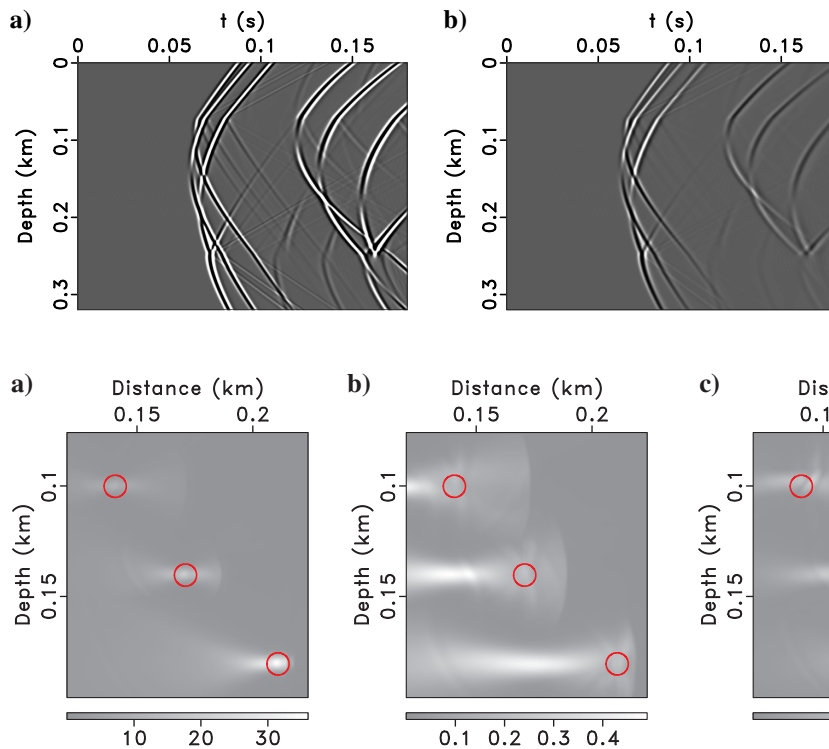

Figure 5. Horizontal displacement for the model in Figure 4. The data are computed for (a) the reference elastic medium, and (b) the viscoelastic medium.

Figure 6. (a) Source images of the elastic data from Figure 5a obtained by elastic time-reversal (ETR). (b-d) Source images of the viscoelastic data from Figure 5b obtained using (b) elastic TR (NVTR), (c) viscoelastic TR with purely isotropic attenuation (IVTR), and (d) viscoelastic TR with the actual anisotropic attenuation (AVTR). A Tukey taper with a cutoff frequency of 800 Hz and taper ratio of 0.2 is applied to stabilize back-propagation. The red circles denote the actual source locations.

Table 1. A Tukey taper with a cutoff frequency of 170 Hz and taper ratio of 0.2 is applied to stabilize back-propagation.

Test 1. Reference test

First, TR is applied to noise-free data recorded in a vertical well by a receiver array with wide aperture (see yellow dots in
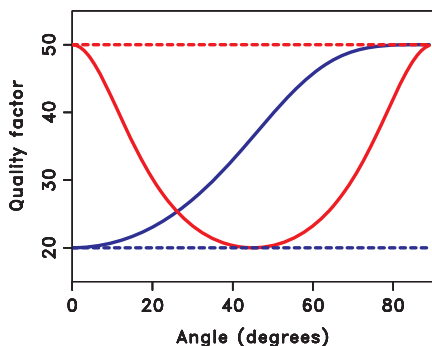

Figure 7. Linearized quality factors of the P- (blue solid curve) and SV-waves (red solid curve) as a function of the phase angle for the second layer from the model in Figure 4. The dashed lines mark the corresponding isotropic quality factors.

Figure 10a). The back-propagation is carried out with the actual velocity model. The reference source images computed by ETR (Figure 10a and 10e) coincide with the actual source locations. NVTR (i.e., no Q-compensation with viscoelastic data) severely underestimates the wavefield energy and produces smeared source locations (Figure 10b and 10f). Isotropic Q-compensation (IVTR) leads to overstated magnitudes and unfocused source images, especially for the two rightmost sources (Figure 10g). For example, the

Table 3. Description of the tests for the BP model.

Test no.	Monitoring array	Velocity	Q	Noise
1	vertical well	accurate	accurate	No
2	surface	accurate	accurate	No
3	vertical well	smoothed	accurate	No
4	vertical well	accurate	smoothed	No
5	vertical well	accurate	accurate	Yes
6	vertical well (limited aperture)	accurate	accurate	No

Note: Each test includes four TR experiments defined in Table 1; "accurate Q" or "smoothed Q" in column 4 applies only to the IVTR and AVTR algorithms.

Figure 8. Time evolution of the field E_S calculated by conducting (a) ETR, (b) NVTR, (c) IVTR, and (d) AVTR; E_S is computed in a circle with a radius of 5 m. The exact excitation times for the three sources in Figure 4 are marked by the black lines, while the estimated times are marked by the red, green, and blue lines (same color as the corresponding sources in Figure 4).
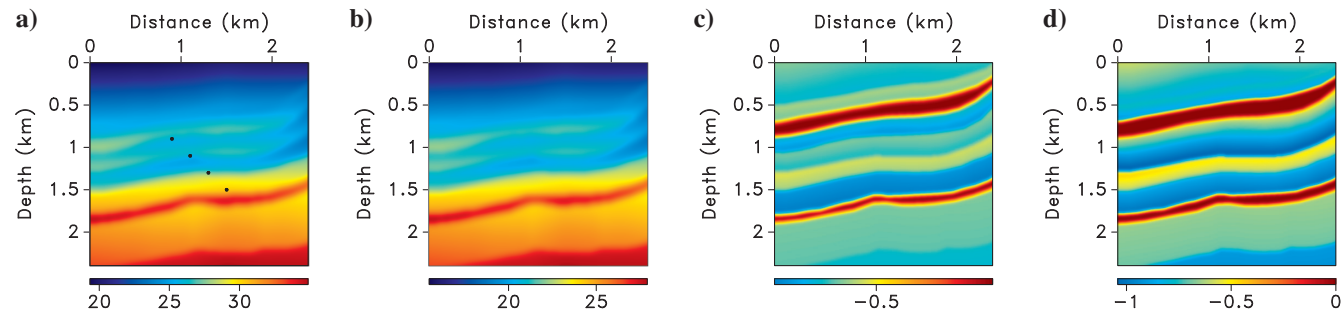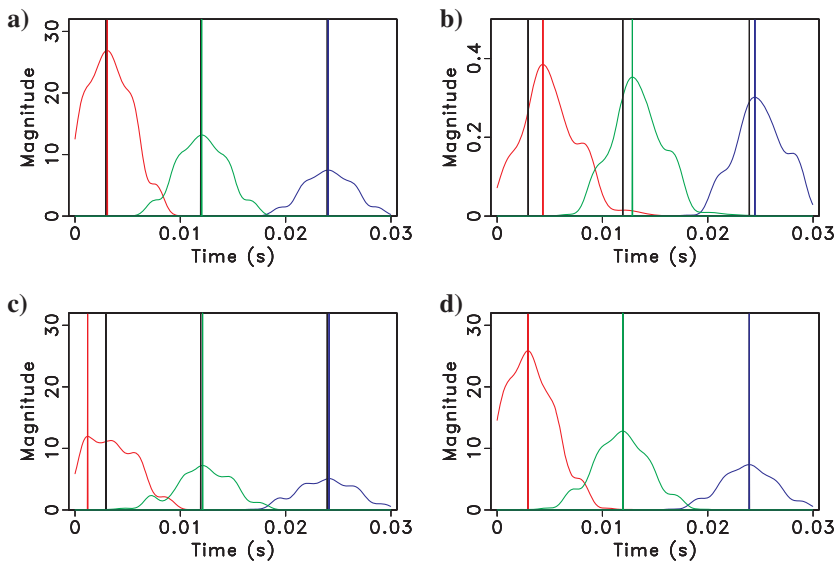
Figure 9. Attenuation parameters for a modified section of the BP TI model: (a) Q_{P0}, (b) Q_{S0}, (c) ε_Q, and (d) δ_Q. The model size is 2.4 km × 2.4 km, with grid spacing $\Delta x = \Delta z = 4$ m. The black dots denote dislocation sources with the excitation time ranging from 72 to 714 ms and the central frequency from 100 to 110 Hz.
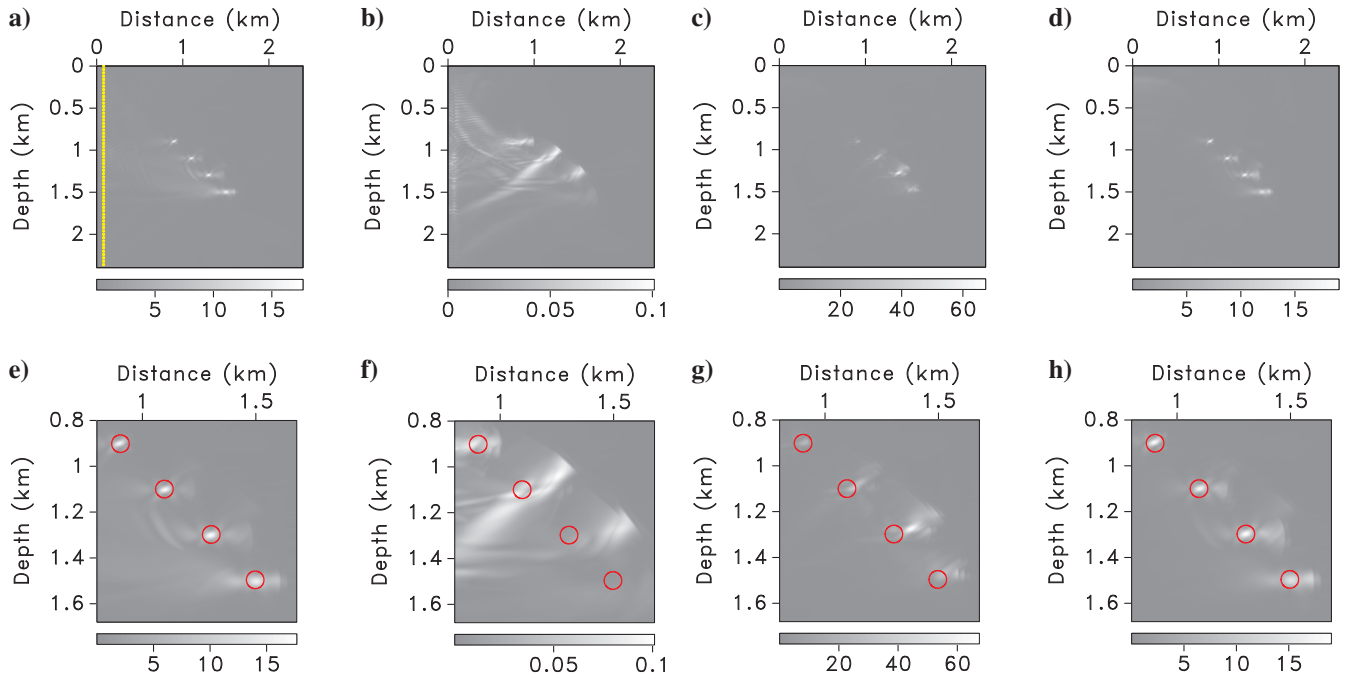
Figure 10. Source images for the model from Figure 9 obtained by (a) ETR, (b) NVTR, (c) IVTR, and (d) AVTR using a vertical receiver array. (e)–(h) The corresponding zoomed-in source areas. The red circles mark the actual source locations. The wavefield is recorded by a vertical array of 60 evenly spaced receivers [yellow dots on plot (a)].
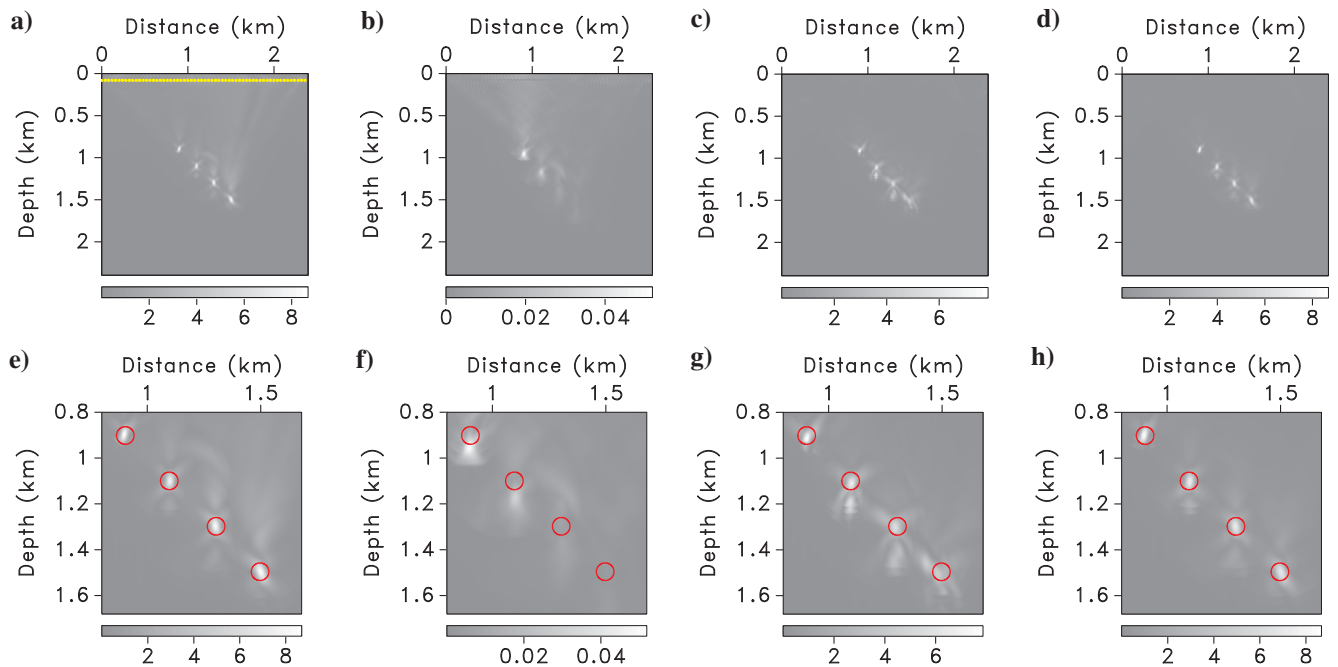

Figure 11. TR results for a horizontal receiver array [yellow dots on plot (a)]. Source images obtained by (a) ETR, (b) NVTR, (c) IVTR, and (d) AVTR using a vertical receiver array. (e)–(h) The corresponding zoomed-in source areas.

image of the third source (we enumerate sources from left to right) is shifted by about 80 m (more than three times the average P-wavelength) from the actual location. Taking the attenuation anisotropy into account (AVTR) generates well-focused and accurately positioned source images (Figure 10h), which are almost indistinguishable from the reference ones (Figure 10e).

Test 2. Surface array

To evaluate the performance of the proposed TR algorithm for surface data, we place the receivers immediately below the surface. As in the previous test, AVTR (Figure 11h) reconstructs the source locations with high accuracy comparable to that of ETR (Figure 11e). NVTR (Figure 11f) distorts the source locations more significantly than in the previous test (Figure 10f) due to the

high attenuation in the shallow layers (Figure 9a and 9b). Isotropic Q-compensation (IVTR) produces better source images than in test 1 (compare Figure 11g with Figure 10g) because wave propagation for this configuration is predominantly near-vertical and the attenuation is relatively well-described by the parameters Q_{P0} and Q_{S0}. Still, correcting for anisotropic attenuation (Figure 11h) enhances the source focusing and provides more accurate source locations.

Test 3. Smoothed velocity model

In the previous two tests, we conducted TR with the actual velocity model. However, imaging (e.g., RTM) is usually performed with a relatively low-resolution velocity field often obtained from reflection tomography. Here, we study the influence of velocity errors on TR images by back-propagating the wavefield through smoothed fields of the parameters V_{P0}, V_{S0}, ε, and δ (Figure 12b); the maximum velocity error is about 8%. As expected, the distorted velocity leads to smearing of the source images (even with ETR) but the maximum focused amplitudes still approximately correspond to source locations (Figure 13a and 13e). As before, AVTR's source images (Figure 13h) are comparable to those by ETR, except for stronger unfocused artifacts produced by AVTR near the third source (from left). IVTR generates much stronger artifacts (Figure 13g), especially for the third and fourth sources, which could lead to serious errors in event location.

Test 4. Smoothed attenuation models

Here, we evaluate distortions in TR images due to inaccurate (smoothed) attenuation models, which are likely to be obtained by conventional attenuation analysis (e.g., by the spectral-ratio

Figure 12. (a) Actual and (b) smoothed fields of the P-wave vertical velocity V_{P0}. The smoothing was performed by a triangle filtering (with a smoothing radius of 20 samples in the vertical and horizontal directions). The same filtering is also applied to the other VTI velocity parameters V_{S0}, ε, and δ (not shown here).
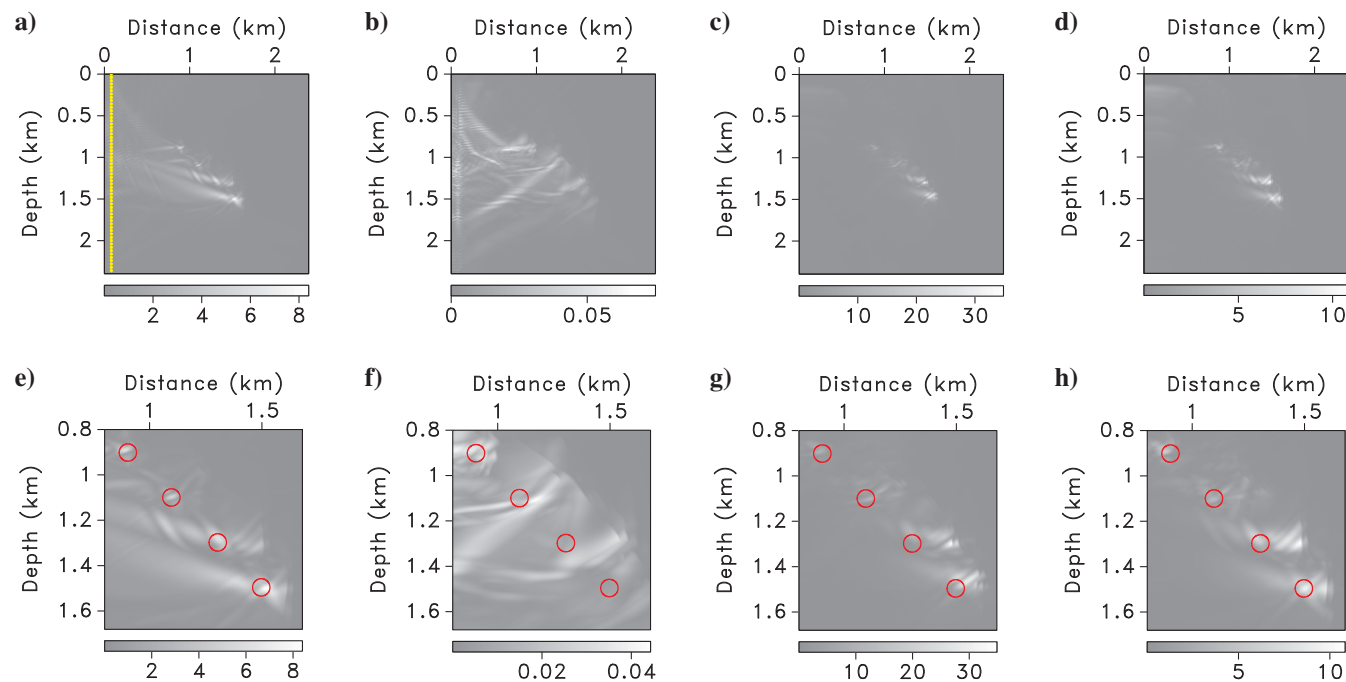

Figure 13. TR results for the smoothed velocity parameters (see Figure 12b). Source images obtained by (a) ETR, (b) NVTR, (c) IVTR, and (d) AVTR using a vertical receiver array. (e)–(h) The corresponding zoomed-in source areas. The wavefield is recorded by a vertical array of 60 evenly spaced receivers [yellow dots on plot (a)].

method). As in test 3, the maximum errors for all four attenuation coefficients are close to 8%. Similar to the results of the previous tests, AVTR produces high-quality source images (Figure 14d), while the IVTR images are smeared and mispositioned (especially for the third and fourth sources, see Figure 14c). This test shows that
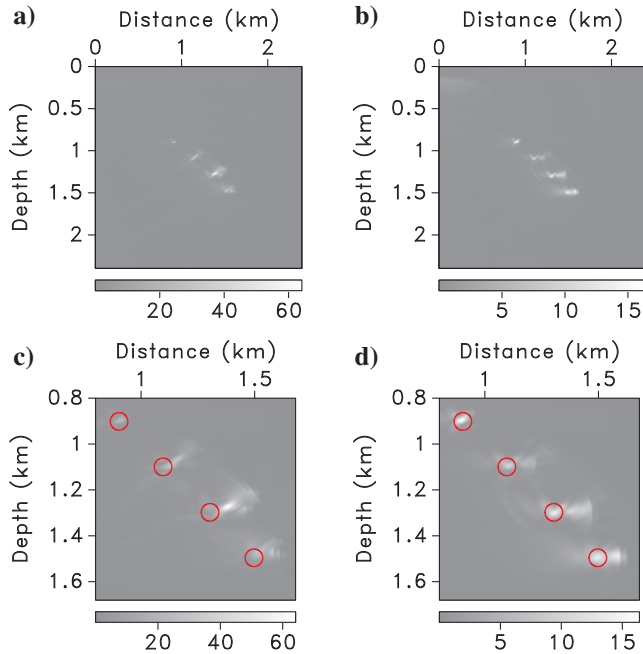

Figure 14. Source images obtained by (a) IVTR, and (b) AVTR using the smoothed attenuation model. (c) and (d) The corresponding zoomed-in source areas.

smoothed *Q*-models might be sufficient for time-reversal imaging, but attenuation anisotropy has to be accounted for.

Test 5. Noise

In the next test, we add band-limited random noise (with the same frequency band as the signal) to the simulated elastic and viscoelastic data (Figure 15). While ETR and NVTR produce almost the same source images (Figure 16a and 16b or Figure 16e and 16f) as the ones in the reference test 1, noise gets substantially amplified after source focusing in IVTR and AVTR, which masks the energy in the source area (Figure 16c and Figure 16d). However, if approximate source locations are known, one can still identify energy focusing in the source area using both IVTR and AVTR (Figure 16g and 16h), although IVTR images are somewhat smeared and mispositioned. Hence, it is essential to suppress noise amplification during *Q*-compensation for avoiding interpretation ambiguities in source localization.

Test 6. Limited aperture

Finally, we examine the dependence of the TR images on the aperture of the receiver array. The length of the receiver array in Figure 10a is reduced from 2.5 km to about 1 km which significantly limits the acquisition aperture (see yellow dots in Figure 17a); also, the spacing between adjacent receivers is increased from 40 m to 72 m. As a result, the source focusing using ETR slightly deteriorates, especially for the third and fourth sources from left (compare Figure 17a with Figure 10a). Similar degradation due to the limited aperture can be observed in the images computed by the other TR algorithms. Still, appropriate compensation for anisotropic attenuation (AVTR; Figure 17d) generates source images that are clearly superior to the output of NVTR (Figure 17b) and IVTR (Figure 17c).
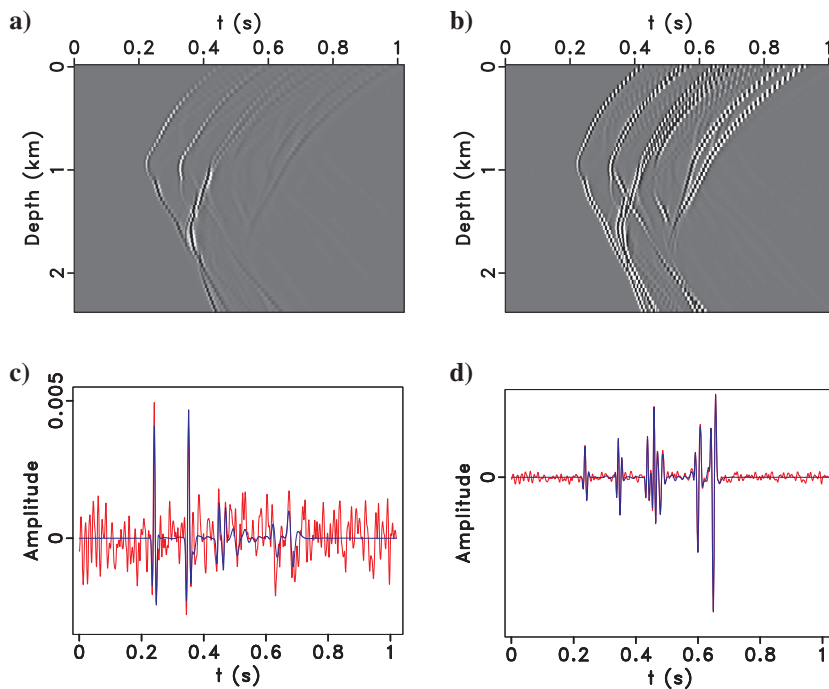

Figure 15. Horizontal displacement for the modified BP section. The data are computed for (a) the viscoelastic medium, and (b) the reference elastic medium. (c) The trace at a depth of 0.8 km from plot (a) (blue curve) and the same trace after the addition of band-limited random noise (red); the approximate signal-to-noise ratio is close to one. (d) The trace at a depth of 0.8 km from plot (b) before (blue curve) and after (red) the addition of the same noise.
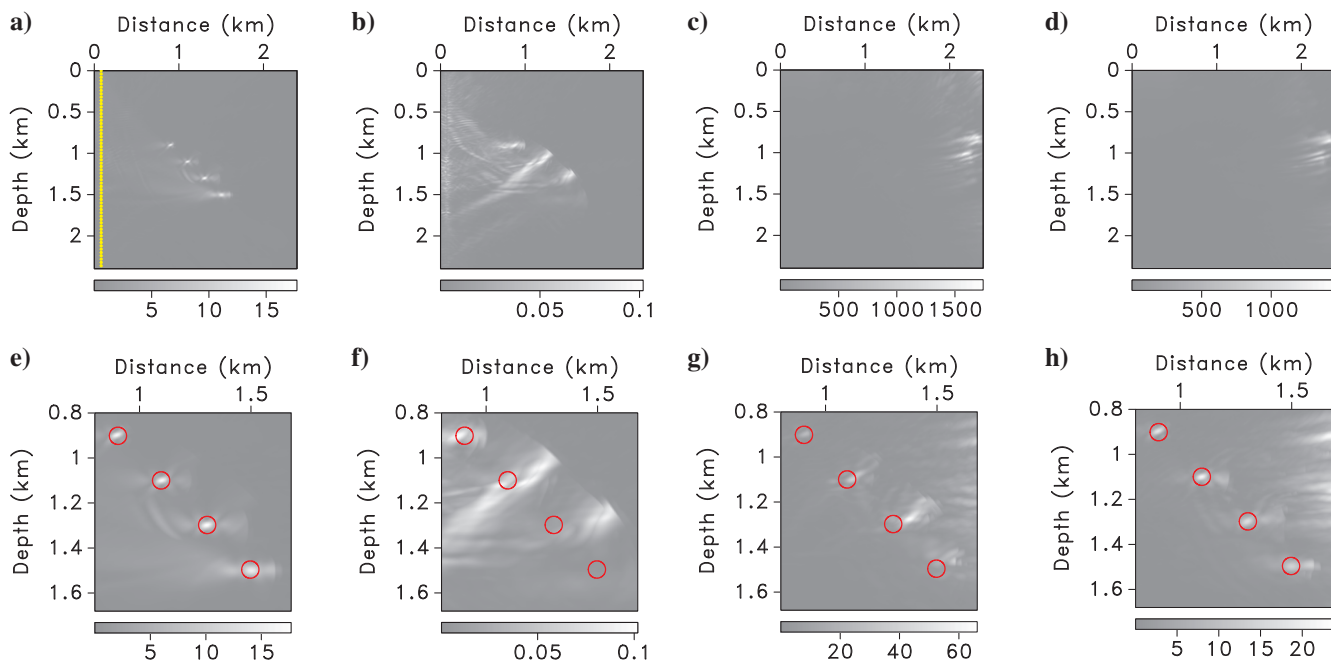
Figure 16. TR results using the noise-contaminated elastic (Figure 15d) and viscoelastic (Figure 15c) data. Source images obtained by (a) ETR, (b) NVTR, (c) IVTR, and (d) AVTR using a vertical receiver array. (e)–(h) The corresponding zoomed-in source areas. The wavefield is recorded by a vertical array of 60 evenly spaced receivers [yellow dots on plot (a)].
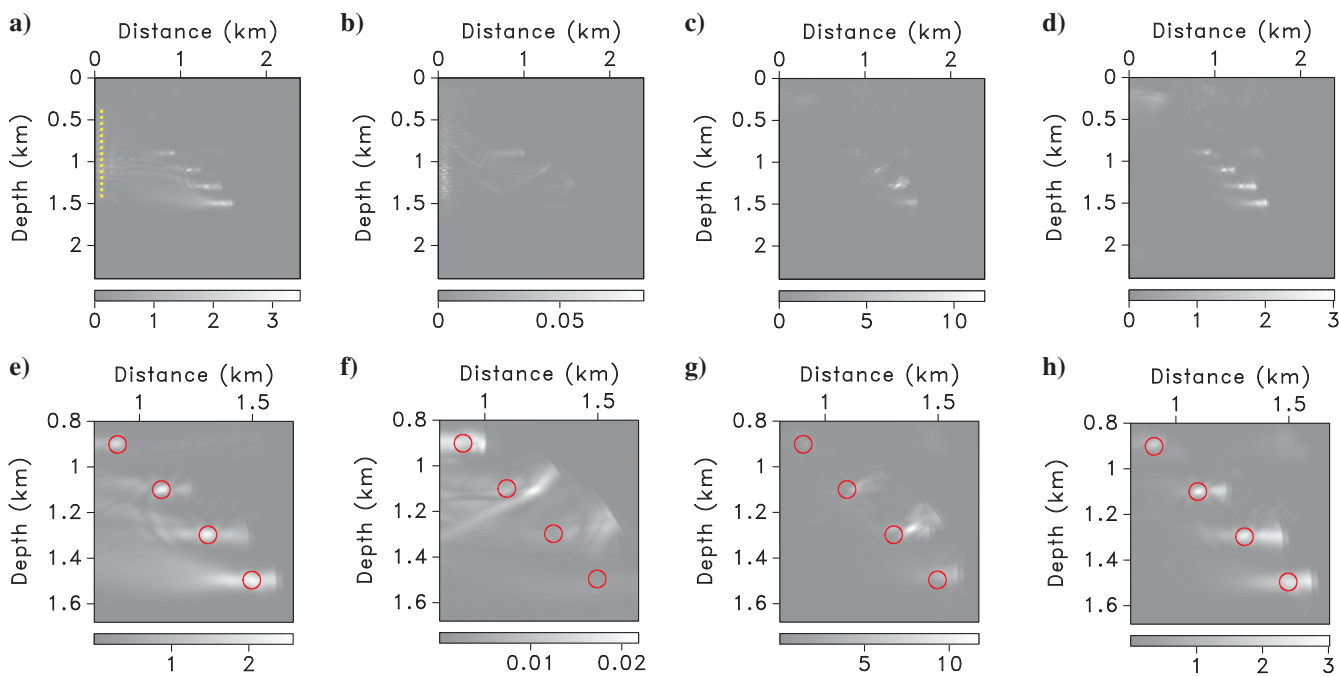

Figure 17. TR results for a shorter receiver array with a larger distance between the receivers [yellow dots on plot (a)]. Source images obtained by (a) ETR, (b) NVTR, (c) IVTR, and (d) AVTR using a vertical receiver array. (e)–(h) The corresponding zoomed-in source areas.

CONCLUSIONS

We presented a method of time-reversal imaging with a visco-elastic VTI wave equation, in which the energy dissipation and velocity dispersion are separated. By changing the signs of the dissipation-related terms while keeping those accounting for

dispersion the same during back-propagation, we compensate for the Q-effect and preserve the time-invariance properties of the wave equation for attenuative anisotropic media. The presence of attenuation anisotropy causes angle-dependent amplitude and traveltime variation even without velocity anisotropy at the reference

frequency. Numerical tests on synthetic viscoelastic microseismic data from a layered VTI model and modified BP TI section validate the *Q*-compensated time-reversal imaging algorithm. It should be emphasized that isotropic *Q*-compensation produces significant distortions in the spatial and temporal source localization for VTI media. In contrast, accounting for attenuation anisotropy leads to superior source images and accurate excitation times, which are comparable to the reference ones obtained for purely elastic media. Therefore, our *Q*-compensated method can potentially provide more accurate microseismic source parameters (locations and excitation times) in unconventional shale plays.

We also used the modified BP model to evaluate the influence of survey geometry, errors in velocity and attenuation, noise, and receiver array aperture on the performance of the proposed method. Our main conclusions are as follows: (1) Attenuation anisotropy plays a more significant role in TR for borehole data than for surface surveys in our tests (with the same recording aperture) for VTI models. (2) Distortions in the anisotropic velocity field can seriously reduce the quality of source focusing, which emphasizes the need to obtain a sufficiently accurate velocity model prior to TR. (3) The spatial resolution of the attenuation model generally does not have a large impact on the TR imaging results. (4) Random noise with the same frequency band as the data gets amplified during *Q*-compensation, which tends to mask the focused energy around the source locations and can cause stability problems. (5) Aperture limitations may lead to deterioration in the source focusing. It should be emphasized that in all our tests TR with anisotropic *Q*-compensation (AVTR) produces results comparable to the reference ones generated by elastic TR of elastic data (ETR), and consistently outperforms the NVTR (no *Q*-compensation) and IVTR (isotropic *Q*-compensation) implementations.

DATA AND MATERIALS AVAILABILITY

Data associated with this research are available and can be obtained by contacting the corresponding author.

APPENDIX A

THOMSEN-STYLE ATTENUATION PARAMETERS FOR P- AND SV-WAVES IN ATTENUATIVE VTI MEDIA

P- and SV-wave propagation in viscoelastic VTI media can be described by the stiffness coefficients C_{ij} (defined at a reference frequency) and the quality-factor elements Q_{ij} ($ij = 11, 13, 33, 55$). However, for estimating velocity and attenuation models, it is more convenient to adopt Thomsen velocity parameters and Thomsen-style attenuation parameters (Zhu and Tsvankin, 2006; Tsvankin and Grechka, 2011). The VTI attenuation parameters for P- and SV-waves are defined as (Zhu and Tsvankin, 2006):

$$A_{P0} \approx \frac{1}{2Q_{P0}} = \frac{1}{2Q_{33}}, \qquad (A-1)$$

$$A_{S0} \approx \frac{1}{2Q_{S0}} = \frac{1}{2Q_{55}}, \qquad (A-2)$$

$$\varepsilon_Q = \frac{Q_{33} - Q_{11}}{Q_{11}}, \qquad (A-3)$$

$$\delta_Q = \frac{1}{2A_{P0}} \frac{d^2 A_P}{d\theta^2} \Big|_{\theta=0^\circ}, \qquad (A-4)$$

where A_P is the P-wave phase attenuation coefficient, θ is the phase angle, A_{P0} and A_{S0} are the symmetry (vertical) attenuation coefficients for P- and SV-waves, ε_Q is the fractional difference between the horizontal and vertical P-wave attenuation coefficients, and δ_Q controls the curvature of A_P in the vertical direction.

REFERENCES

Ammari, H., E. Bretin, J. Garnier, and A. Wahab, 2013, Time-reversal algorithms in viscoelastic media: European Journal of Applied Mathematics, **24**, 565–600, doi: 10.1017/S0956792513000107.

Artman, B., I. Podladtchikov, and B. Witten, 2010, Source location using time-reverse imaging: Geophysical Prospecting, **58**, 861–873, doi: 10.1111/j.1365-2478.2010.00911.x.

Bai, T., and I. Tsvankin, 2016, Time-domain finite-difference modeling for attenuative anisotropic media: Geophysics, **81**, no. 2, C69–C77, doi: 10.1190/geo2015-0424.1.

Bai, T., I. Tsvankin, and X. Wu, 2017, Waveform inversion for attenuation estimation in anisotropic media: Geophysics, **82**, no. 4, WA83–WA93, doi: 10.1190/geo2016-0596.1.

Baysal, E., D. D. Kosloff, and J. W. Sherwood, 1983, Reverse time migration: Geophysics, **48**, 1514–1524, doi: 10.1190/1.1441434.

Behura, J., I. Tsvankin, E. Jenner, and A. Calvert, 2012, Estimation of interval velocity and attenuation anisotropy from reflection data at Coronation field: The Leading Edge, **31**, 580–587, doi: 10.1190/tle31050580.1.

Best, A. I., J. Sothcott, and C. McCann, 2007, A laboratory study of seismic velocity and attenuation anisotropy in near-surface sedimentary rocks: Geophysical Prospecting, **55**, 609–625, doi: 10.1111/j.1365-2478.2007.00642.x.

Bohlen, T., 2002, Parallel 3-D viscoelastic finite difference seismic modelling: Computers and Geosciences, **28**, 887–899, doi: 10.1016/S0098-3004(02)00006-7.

Carcione, J. M., 1993, Seismic modeling in viscoelastic media: Geophysics, **58**, 110–120, doi: 10.1190/1.1443340.

Carcione, J. M., 2008, Theory and modeling of constant-Q P-and S-waves using fractional time derivatives: Geophysics, **74**, no. 1, T1–T11, doi: 10.1190/1.3008548.

Carcione, J. M., F. Cavallini, F. Mainardi, and A. Hanyga, 2002, Time-domain modeling of constant-Q seismic waves using fractional derivatives: Pure and Applied Geophysics, **159**, 1719–1736, doi: 10.1007/s00024-002-8705-z.

Emmerich, H., and M. Korn, 1987, Incorporation of attenuation into time-domain computations of seismic wave fields: Geophysics, **52**, 1252–1264, doi: 10.1190/1.1442386.

Fink, M., and C. Prada, 2001, Acoustic time-reversal mirrors: Inverse Problems, **17**, R1, doi: 10.1088/0266-5611/17/1/201.

Gajewski, D., and E. Tessmer, 2005, Reverse modelling for seismic event characterization: Geophysical Journal International, **163**, 276–284, doi: 10.1111/j.1365-246X.2005.02732.x.

Galvin, R. J., and B. Gurevich, 2015, Frequency-dependent anisotropy of porous rocks with aligned fractures: Geophysical Prospecting, **63**, 141–150, doi: 10.1111/1365-2478.12177.

Guo, P., and G. A. McMechan, 2017, Sensitivity of 3D 3C synthetic seismograms to anisotropic attenuation and velocity in reservoir models: Geophysics, **82**, no. 2, T79–T95, doi: 10.1190/geo2016-0321.1.

Guo, P., G. A. McMechan, and H. Guan, 2016, Comparison of two viscoacoustic propagators for Q-compensated reverse time migration: Geophysics, **81**, no. 5, S281–S297, doi: 10.1190/geo2015-0557.1.

Kremers, S., A. Fichtner, G. Brietzke, H. Igel, C. Larmat, L. Huang, and M. Kaser, 2011, Exploring the potentials and limitations of the time-reversal imaging of finite seismic sources: Solid Earth, **2**, 95–105, doi: 10.5194/se-2-95-2011.

Labyed, Y., and L. Huang, 2012, Ultrasound time-reversal MUSIC imaging with diffraction and attenuation compensation: IEEE Transactions on Ultrasonics, Ferroelectrics, and Frequency Control, **59**, doi: 10.1109/TUFFC.2012.2445.

Larmat, C., J.-P. Montagner, M. Fink, Y. Capdeville, A. Tourin, and E. Clévédé, 2006, Time-reversal imaging of seismic sources and application to the great Sumatra earthquake: Geophysical Research Letters, **33**, doi: 10.1029/2006GL026336.

Li, Z., and M. van der Baan, 2016, Microseismic event localization by acoustic time reversal extrapolation: Geophysics, **81**, no. 3, KS123–KS134, doi: 10.1190/geo2015-0300.1.

McMechan, G. A., 1982, Determination of source parameters by wavefield extrapolation: Geophysical Journal International, **71**, 613–628, doi: 10.1111/j.1365-246X.1982.tb02788.x.

McMechan, G. A., 1983, Migration by extrapolation of time-dependent boundary values: Geophysical Prospecting, **31**, 413–420, doi: 10.1111/j.1365-2478.1983.tb01060.x.

Qi, Q., T. M. Müller, and M. Pervukhina, 2017, Sonic Q_P/Q_S ratio as diagnostic tool for shale gas saturation: Geophysics, **82**, no. 3, MR97–MR103, doi: 10.1190/geo2016-0499.1.

Steiner, B., E. H. Saenger, and S. M. Schmalholz, 2008, Time reverse modeling of low-frequency microtremors: Application to hydrocarbon reservoir localization: Geophysical Research Letters, **35**, doi: 10.1029/2007GL032097.

Tsvankin, I., and V. Grechka, 2011, Seismology of azimuthally anisotropic media and seismic fracture characterization: SEG.

Zhu, T., 2014, Time-reverse modelling of acoustic wave propagation in attenuating media: Geophysical Journal International, **197**, 483–494, doi: 10.1093/gji/ggt519.

Zhu, T., 2015, Viscoelastic time-reversal imaging: Geophysics, **80**, no. 2, A45–A50, doi: 10.1190/geo2014-0327.1.

Zhu, T., 2017, Numerical simulation of seismic wave propagation in viscoelastic-anisotropic media using frequency-independent Q wave equation: Geophysics, **82**, no. 4, WA1–WA10, doi: 10.1190/geo2016-0635.1.

Zhu, T., and T. Bai, 2019, Efficient modeling of wave propagation in a vertical transversely isotropic attenuative medium based on fractional Laplacian: Geophysics, **84**, no. 3, T121–T131, doi: 10.1190/geo2018-0538.1.

Zhu, T., and J. M. Carcione, 2014, Theory and modelling of constant-Q P- and S-waves using fractional spatial derivatives: Geophysical Journal International, **196**, 1787–1795, doi: 10.1093/gji/ggt483.

Zhu, T., and J. M. Harris, 2014, Modeling acoustic wave propagation in heterogeneous attenuating media using decoupled fractional Laplacians: Geophysics, **79**, no. 3, T105–T116, doi: 10.1190/geo2013-0245.1.

Zhu, T., and J. Sun, 2017, Viscoelastic reverse time migration with attenuation compensation: Geophysics, **82**, no. 2, S61–S73, doi: 10.1190/geo2016-0239.1.

Zhu, Y., and I. Tsvankin, 2006, Plane-wave propagation in attenuative transversely isotropic media: Geophysics, **71**, no. 2, T17–T30, doi: 10.1190/1.2187792.

Zhu, Y., I. Tsvankin, P. Dewangan, and K. van Wijk, 2006, Physical modeling and analysis of P-wave attenuation anisotropy in transversely isotropic media: Geophysics, **72**, no. 1, D1–D7, doi: 10.1190/1.2374797.

Zhubayev, A., M. E. Houben, D. M. Smeulders, and A. Barnhoorn, 2015, Ultrasonic velocity and attenuation anisotropy of shales, Whitby, United Kingdom: Geophysics, **81**, no. 1, D45–D56, doi: 10.1190/geo2015-0211.1.